Optical Engineering

OpticalEngineering.SPIEDigitalLibrary.org

Image reconstruction for single detector rosette scanning systems based on compressive sensing theory

Hande Uzeler
Serdar Cakir
Tayfun Aytaç

SPIE.

Image reconstruction for single detector rosette scanning systems based on compressive sensing theory

Hande Uzeler,* Serdar Cakir, and Tayfun Aytaç
TÜBİTAK BİLGEM İLTAREN, Şehit Yzb. İlhan Tan Kışlası, 2432. cad., 2489. sok., TR-06800 Ümitköy, Ankara, Turkey

Abstract. Compressive sensing (CS) is a signal processing technique that enables a signal that has a sparse representation in a known basis to be reconstructed using measurements obtained below the Nyquist rate. Single detector image reconstruction applications using CS have been shown to give promising results. In this study, we investigate the application of CS theory to single detector infrared (IR) rosette scanning systems which suffer from low performance compared to costly focal plane array (FPA) detectors. The single detector pseudoimaging rosette scanning system scans the scene with a specific pattern and performs processing to estimate the target location without forming an image. In this context, this generation of scanning systems may be improved by utilizing the samples obtained by the rosette scanning pattern in conjunction with the CS framework. For this purpose, we consider surface-to-air engagement scenarios using IR images containing aerial targets and flares. The IR images have been reconstructed from samples obtained with the rosette scanning pattern and other baseline sampling strategies. It has been shown that the proposed scheme exhibits good reconstruction performance and a large size FPA imaging performance can be achieved using a single IR detector with a rosette scanning pattern. © *2016 Society of Photo-Optical Instrumentation Engineers (SPIE)* [DOI: 10.1117/1.OE.55.2.023108]

Keywords: image reconstruction; infrared imaging; infrared detectors; optical systems; imaging systems.

Paper 150683P received May 30, 2015; accepted for publication Jan. 25, 2016; published online Feb. 26, 2016.

1 Introduction

The compressive sensing (CS) framework states that a compressible signal may be reconstructed from samples that have been obtained below the Nyquist sampling rate. In conventional imaging systems, the acquired data are generally compressed before saving and further processing. An image $I \in \mathbb{R}^N$, which has a sparse representation in a given basis, may be represented as the linear combination of K coefficients, where $K \ll N$. Thus, compressing an image is achieved by computing K coefficients from N pixel values and saving their values and locations. When image sampling and compression are performed in this manner, much of the sampled data are discarded. However, if the signal is compressible in a given basis, the acquisition of the signal in a compressed form without first sampling the whole signal and the subsequent reconstruction has been made possible by CS.[1,2]

CS theory has found uses in various applications. The theory is widely used in medical applications such as x-ray imaging[3] and magnetic resonance imaging.[4] Another active area is radar system design,[5] synthetic aperture radar imaging,[6] and radar remote sensing.[7] Other applications include the detection of changes and moving objects,[8,9] electro-optic and infrared (IR) applications,[10] hyperspectral imaging,[11] image fusion,[12] super-resolution imaging,[13] and image recovery.[14] A comprehensive survey on the applications of CS can be found in Ref. 15.

CS can also be used in data acquisition problems because the framework permits compressed measurements to be taken from the data. This principle has been applied to an imaging device and an image reconstruction method using a single detector has been presented in Ref. 16. This imaging device utilizing a single photon detector reduces the number of measurements which need to be taken from the image while still providing high spatial resolution. The single pixel camera architecture may also be adapted to be used at other wavelengths, such as IR. This work has been extended by Mahalanobis et al.[17] where the authors developed a CS testbed which uses a 4096×2048 pixels spatial light modulator to produce a 4096×2048 pixels scene with a 128×64 pixels focal plane array (FPA). It has been shown that a higher spatial resolution can be achieved from measurements made with a small size FPA.

IR detectors are used in IR-guided missile seekers, where the IR seeker estimates the position of the target within its field of view (FOV) by detecting and processing the IR energy radiated from the target. IR seekers can be classified into the nonimaging, semi-imaging, and imaging seeker categories based on their imaging technologies.

Nonimaging IR seekers are the oldest type of IR seekers in which the IR scene is modulated by a reticle which can be rotating or stationary. These reticle seekers suffer from low performance, especially when there are multiple targets such as flares within their FOV.[18]

Semi-imaging seekers scan the total FOV (TFOV) in a specific pattern with the help of a single detector and an optical scanning system. The detector has a very small instantaneous FOV (IFOV). In this manner, at the end of the scan period, a partial image of the scene is obtained. To perform target position estimation, the radiance values of sampled spatial locations from the scene are processed directly without forming an actual image.[19] An example of semi-imaging seekers is the rosette scanning seeker.

*Address all correspondence to: Hande Uzeler, E-mail: hande.uzeler@tubitak.gov.tr

0091-3286/2016/$25.00 © 2016 SPIE

Imaging IR seekers have been developed in parallel with the advances in IR detector technology. The single detector or detector arrays which scanned the scene in earlier generations have been replaced by two-dimensional staring FPAs in imaging seekers, enabling the seeker to acquire the IR scene as an image. While they provide higher resolution with higher imaging performance, and permit the use of advanced image processing and target detection algorithms, these imaging IR seekers are quite expensive. In the IR band, where it is expensive to acquire raw image data, CS can be used to convert the signals obtained by a single IR detector into images.

In the single detector rosette scanning seekers, the seeker samples the IR scene with a specific scanning pattern, but instead of forming an image with the acquired samples, other signal processing techniques are employed to estimate the target's position. The CS framework may enable the reconstruction of the samples obtained by the seeker to form an image for target acquisition, detection, and tracking purposes.

In this work, the signals obtained by the scanning pattern in rosette scanning seekers are reconstructed using CS. Our main motivation is to investigate the possible improvement of already existing rosette scanning seekers and to seek possible applications of CS theory to semi-imaging IR seekers. Different sampling strategies are used to acquire the CS measurements, and image reconstruction was performed. These sampling strategies represent the baseline strategies for comparison purposes. This paper is an extension of our previous works.[20,21] In Ref. 20, the sampling model of the rosette scanning seeker was a point-based model and we considered sea–surface targets. In this paper, the point-based sampling model is modified to a circular spot model to provide more realistic simulation results. We also focus on surface-to-air engagement scenarios, hence the targets are airborne. Moreover, the proposed reconstruction framework is also tested using IR images containing an airborne target which uses flares as a countermeasure technique. The paper is organized as follows: Sec. 2 provides an overview of CS and single-detector imaging. In Sec. 3, the scanning pattern employed in rosette scanning seekers and the rosette measurement matrix are discussed. Section 4 provides the experimental methodology, recovery results, and comparative analysis.

2 Compressive Sensing

A compressible signal may be reconstructed from a small set of linear nonadaptive measurements using the CS framework. The signal x in $\mathbb{R}^N$ may be represented in terms of basis vectors $\{\psi_i\}_{i=1}^N$, where each vector has size $N \times 1$. If the signal is an image, it is vectorized into a one-dimensional signal. The signal x may be represented using the $N \times N$ basis matrix $\Psi = [\psi_1 | \psi_2 | \ldots | \psi_N]$ as

$$x = \Psi s. \tag{1}$$

The signal x may be represented as the linear combination of only K basis vectors if there are only K ($K \ll N$) nonzero coefficients in the $N \times 1$ vector s. Therefore, x is a K-sparse signal in the Ψ domain.

CS enables the reconstruction of the signal x from $M < N$ measurements without the need to compute K coefficients. The measurements $y(m)$, $m \in \{1,2,\ldots,M\}$, are equal to the inner product of x with M vectors $\{\phi_j\}_{j=1}^M$ such that $y(m) = \langle x, \phi_m^T \rangle$. By arranging the measurement vectors as rows of the matrix Φ, the $M \times 1$ measurement data vector may be represented as[22]

$$y = \Phi x = \Phi \Psi s. \tag{2}$$

The reconstruction algorithm uses the measurement matrix Φ, the sparsity basis matrix Ψ, and the M measurements in y to reconstruct the $N \times 1$ signal s, which is the sparse representation of the signal x. Since $M < N$, the recovery of x from y is usually ill-posed. Reconstruction is possible due to the sparsity of the signal x and the incoherence of the matrices Φ and Ψ. When the elements of the measurement matrix Φ are chosen to have normal or Bernoulli distributions, it has been shown that they achieve the incoherence condition with a high probability for any choice of the orthonormal basis Ψ.[23]

The recovery of the sparse signal s is carried out by finding the vector $\hat{s}$ which satisfies the M measurements in y while minimizing the ℓ_0-norm. Solving this ℓ_0-norm minimization problem is a complex problem and one of the most important contributions made by the CS theory is that it is possible to reconstruct the signal through ℓ_1-norm minimization. Therefore, the signal may be reconstructed by solving the minimization problem given in Eq. (3). This optimization problem is also known as basis pursuit and can be solved by linear programming techniques.[16]

$$\hat{s} = \arg\ \min \|s'\|_1 \text{s.t.} y = \Phi \Psi s'. \tag{3}$$

2.1 *Single-Detector Imaging*

In Ref. 16, a single-detector imaging system has been presented. The single pixel camera shown in Fig. 1 consists of a single detector and a microcontrolled digital micromirror device (DMD) which can be operated according to a pseudorandom or a given measurement basis. The mirror orientations are modulated according to M pseudorandom measurement patterns ϕ_m such that M measurements are taken from the image. The image to be reconstructed is formed on the DMD plane and focused by a lens onto the detector where the signal is summed. Each mirror configuration yields a different measurement value $y(m)$ on the detector, which is equal to the inner product of the image x with the measurement basis vector ϕ_m. In this manner, M incoherent projections of an image which has N pixels are acquired without directly sampling the N pixel values. Therefore, at wavelengths where imaging is prohibitively expensive, an imaging system utilizing a single detector may be realized with the help of this framework.

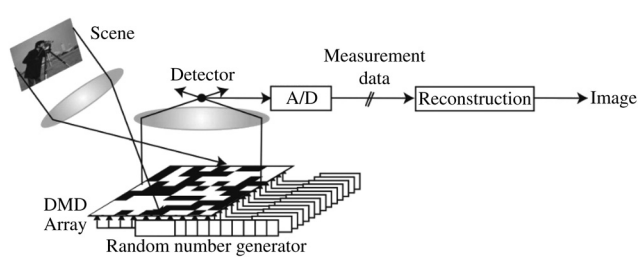

Fig. 1 Single pixel camera architecture.[16]

For each measurement, the configuration of the DMD is changed by the pseudorandom number generator such that the orientation of the mirrors may either reflect the light toward the detector or away from it. In this system architecture, each measurement is the inner product of the image and a Bernoulli distributed random matrix. The number of Bernoulli distributed matrices realized on the DMD is equal to the number of samples that we wish to obtain from the image to be reconstructed. In relation to Eq. (2), each row of the measurement matrix Φ is the vectorized form of a Bernoulli distributed matrix realized on the DMD. Therefore, the construction of the measurement matrix associated with sampling the scene via the DMD is carried out by generating Bernoulli distributed random matrices.

3 Rosette Scanning Pattern

Rosette scanning systems scan the scene using a fixed scanning pattern through a small IFOV and process the signal at the detector to yield the position information of the target. As an example of the scanning pattern, the IFOV and TFOV of a rosette scanning seeker are shown in Fig. 2.

Scanning is performed by two tilted prisms, mirrors, or lenses which are spinning at two different frequencies f_1 and f_2 as shown in Fig. 3. The rosette scanner uses prisms with apex angles ϕ_1 and ϕ_2. Different values of f_1 and f_2 produce different scanning patterns.

The location of the center of the IFOV at time t is calculated as shown in Eq. (4)[19] where ρ is the deviation angle of the prism and the radius of the TFOV, i.e., the radius of the circle formed by the outermost points of the rosette pattern.

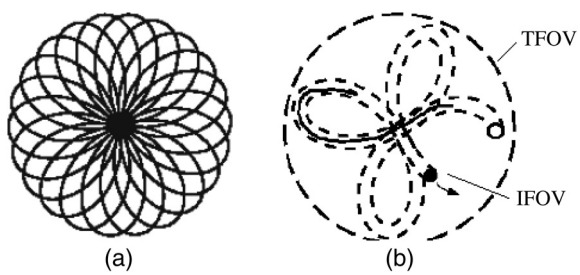

Fig. 2 (a) Rosette scanning pattern and (b) the illustration of TFOV and IFOV.

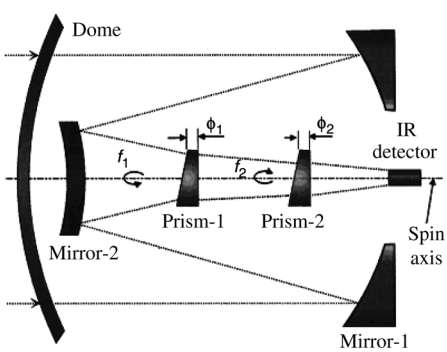

Fig. 3 Rosette scanning system architecture.[24]

$$x(t) = \frac{\rho}{2}[\cos(2\pi f_1 t) + \cos(2\pi f_2 t)]$$
$$y(t) = \frac{\rho}{2}[\sin(2\pi f_1 t) - \sin(2\pi f_2 t)]. \quad (4)$$

The number of petals present in the pattern is computed as $N = N_1 + N_2$, where $N_1 = f_1/f$, $N_2 = f_2/f$, and f_1 and f_2 have the greatest common divisor f. The rosette scanner completes one scan in $T = 1/f$ s. The size of the IFOV is represented as

$$\omega = \tfrac{2\pi}{N}\rho\,\cos(\pi/\Delta N)\,, \quad (5)$$

where $\Delta N = N_1 - N_2$.[19] Due to the scanning architecture, the IFOV passes through the center of the TFOV many times as shown in Fig. 2. Therefore, sampling in the center is denser compared to the edges as shown in Fig. 2.

At the end of the scan period, the pulses of the modulated signal at the detector output are processed to perform the position estimation of the target. The sampling rate of the detector output determines how many samples are taken from the scene in one scanning period. According to the occurrence time of the pulse, position information is generated using Eq. (4). After all of the pulses have been processed, the pulses may be grouped using the ISODATA technique to obtain the spatial position estimate of the target.[25]

3.1 *Rosette Measurement Matrix*

For the construction of the measurement matrix associated with the rosette scanning seeker architecture, a rosette scanning pattern was constructed for $f_1 = 275$ Hz and $f_2 = 175$ Hz. The rosette scanning pattern was constructed using the IFOV motion relation stated in Eq. (4) for a given sampling rate. In order to gather different numbers of measurements from the image for reconstruction, the sampling rate of the rosette pattern needs to be changed. This is accomplished by sampling the detector outputs with different sampling rates which are chosen as 39.6, 63.2, and 102 kHz in this study. The generated patterns, in increasing sampling rate order, for these sampling rates are shown in Fig. 4, and the number of samples obtained is stated.

At each time instant, the detector samples the scene through its IFOV. In a rosette pattern, the center point's location is given by Eq. (4) and the width of the IFOV is given by Eq. (5). Therefore, every sample taken from the scene is the sum of many irradiance values which are contained within the IFOV. An example of the rosette scanning pattern and the samples taken from an IR test image is shown in Fig. 5. In Fig. 5(b), the rosette scanning pattern is given for 1588 samples and each point in the pattern corresponds to the center of the IFOV. A certain IFOV center location is represented as a rectangular point in Fig. 5(b) and its corresponding IFOV region is shown in Fig. 5(c). The IR test image is shown in Fig. 5(a), and the samples taken from the image for the IFOV center location given in Fig. 5(b) are shown in Fig. 5(d). In the context of CS, the scanning architecture of the rosette scanner can be thought of as similar to the single pixel camera in the sense that it enables measurements to be taken from the scene with a certain pattern.

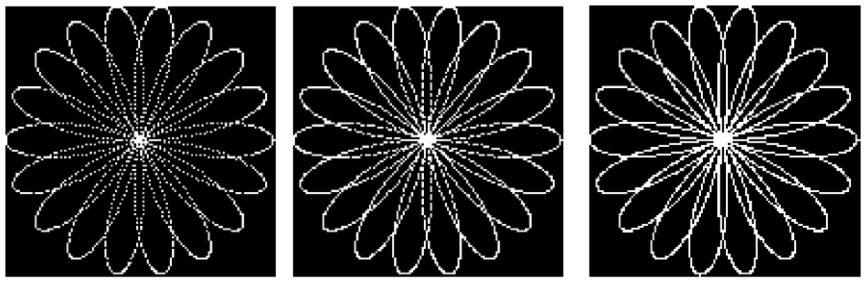

(a) (b) (c)

Fig. 4 Rosette scanning patterns which take (a) 1588 samples, (b) 2532 samples, and (c) 4082 samples.

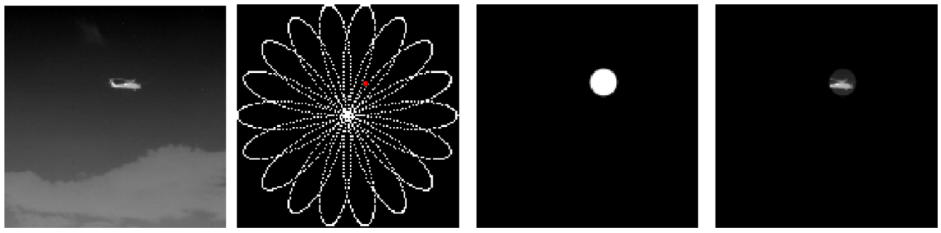

(a) (b) (c) (d)

Fig. 5 (a) The test image, (b) the rosette scanning pattern, (c) the IFOV region, and (d) the samples obtained from the test image for the given IFOV location.

The rosette scanning seeker takes one measurement from the scene for every IFOV center point present in the rosette scanning pattern. Because the IFOV is not a single point (as considered in Ref. 20) but rather a circular region, every measurement includes information about the region of the scene where the detector IFOV is looking at instantaneously. Therefore, each measurement contains information from many pixels. For every measurement, we must form a rosette scanning pattern matrix which corresponds to the circular IFOV region, so that we can sample only that part of the scene. The image, which can also be visualized as a matrix as shown in Fig. 5(c), is an example of the rosette scanning pattern matrix for one IFOV center location. This matrix is formed using the center location and size of the IFOV. For this IFOV region, the pixel location of each point within the IFOV is calculated. If this point lies completely within the IFOV region, the value at that pixel location is set to one. If the point is not completely within the IFOV but intersects the IFOV region, the amount of intersection is computed and that value is set at the pixel location. The remaining values in the rosette scanning pattern matrix are set to zero. By using this circular IFOV approach to construct the measurement matrix it is possible to extract more information from the scene with each measurement since each measurement contains information about a region rather than a single point. The rosette measurement matrix, which corresponds to the Φ in the CS framework, is formed by vectorizing for each rosette scanning pattern matrix, the IFOV locations of the rosette pattern and placing it as the m'th row of the measurement matrix.

It can be observed from Fig. 5(c) that the rosette scanning pattern matrix contains only a limited number of nonzero values. The IFOV region can be seen in detail in Fig. 6(a) and the histogram of the nonzero values of the IFOV region can be seen in Fig. 6(b). The IFOV diameter shown in Fig. 6(a) is 16 pixels. The number of elements equal to

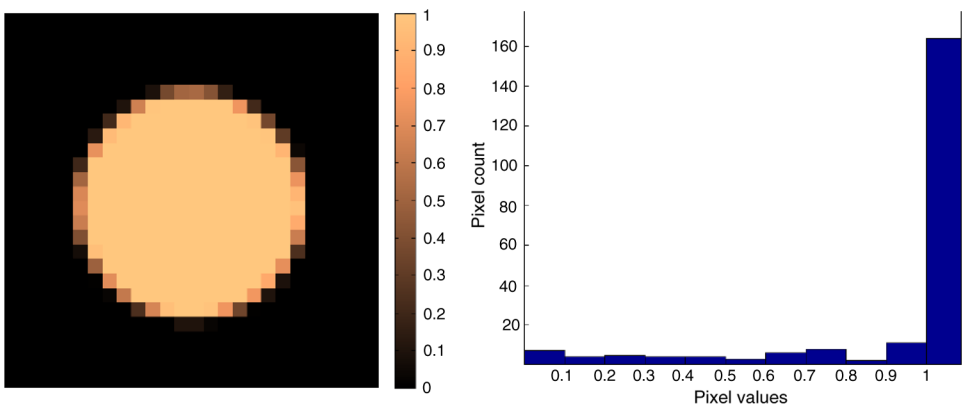

(a) (b)

Fig. 6 (a) The IFOV pixel values and (b) histogram of values between zero and one.

one is 164 and the number of elements whose values are between zero and one is equal to 57. Therefore, ~1.3% of the elements present in the rosette scanning pattern matrix are nonzero. When the IFOV center point is near the edge of the TFOV, the IFOV region can be smaller than the region shown in Fig. 5(c). On average, the IFOV region contains 160 elements equal to one and 53 elements whose values are between zero and one.

4 Experiments

In this work, the detector outputs from a single detector rosette scanning seeker have been reconstructed via CS for different numbers of samples taken from the IR image using computer simulations. The IR images to be reconstructed are of size 128×128. These images have been obtained by a stationary long-wave IR camera working in the 8–12 μm band. Although most of the surface-to-air seekers considered in this study are known to operate in the mid-wave IR band, the images used in the experiments are representative for testing purposes. Our test image dataset consists of 460 IR images captured in different weather conditions with various different target ranges and target orientations.

In addition, to obtain a more controlled environment, synthetic images have been generated. Some of the synthetic test images also contain flares. Our main motivation for generating synthetic images is to observe the system performance in the case of multiple IR sources in the scene, such as a flare and an air platform, which is a realistic engagement between a seeker and a platform. The synthetic images are generated such that the airborne target makes translational and rotational movements within the FOV. In the synthetic images containing a flare, the flare is modeled as a Gaussian source. The flare also makes translational and rotational movements in the scene. In this work, our aim is not to implement a closed-loop missile simulation, so missile motion with respect to the target is not considered. We only generate the scene as the missile would observe it at a given time instant. Our synthetic test image dataset consists of 400 images, half of which contain a flare.

The reconstruction of a signal from samples obtained via CS can be carried out using one of the many open source software packages developed for this task.[26–28] In this work, the basis pursuit method in the SPGL1 library is used to recover the images.[28,29] The sparsity basis Ψ is chosen as the discrete Fourier transform matrix. The measurement matrix Φ is constructed according to the measurement method. Three different methods, the rosette sampling pattern method and two random sampling methods, are used to take the measurements. The random sampling methods are sampling with Bernoulli random matrices, which can be implemented via a DMD, and the random Gaussian sampling method. We compare the reconstruction performance of the rosette sampling method to the random sampling methods because they can be considered as baseline sampling techniques which have been used in the literature.

The construction procedure of the random Bernoulli measurement matrix which consists of Bernoulli distributed random variables to be used with the DMD is provided in Sec. 2.1. For the construction of the random Gaussian sampling measurement matrix, a similar procedure is followed where instead of generating Bernoulli distributed matrices, random matrices where the elements have a standard normal distribution are generated. The construction procedure of the rosette measurement matrix is provided in Sec. 3.1. It should also be noted that, unlike the random Bernoulli and random Gaussian sampling techniques, the measurement matrix obtained with the rosette scanning pattern does not have any randomness associated with it. Due to the nature of the rosette scanning mechanism, the coherency between the consecutive sampling instances is high. Since the seeker collects the signal within its IFOV and the IFOV regions located in the same neighborhood overlap significantly, the samples collected from these IFOV regions contain coherent information. To use the SPGL1 library for this optimization problem, the measurement matrices are suggested to be orthonormalized beforehand. Therefore, in order to solve the optimization problem efficiently, an orthonormalization process is carried out using the Gram–Schmidt algorithm for the measurement matrix. Therefore, the measurement matrices satisfy the restricted isometric property after the orthonormalization process.

4.1 *Performance of the Proposed Scheme*

The rosette scanning pattern, due to its scanning structure as mentioned in Sec. 3, takes more samples from the center of its FOV. As the sampling rate increases, the number of samples taken from the center increases. In the case where the target is near the center of the FOV, the rosette sampling pattern will take many samples from the target. Therefore, to make fair comparisons when comparing the performance of the rosette scanning seeker, we also use test images in which the target is not directly in the center of the FOV.

Figure 7 shows some test images from the dataset and the reconstructed images with the rosette measurement matrix. The number of measurements taken from the image is 2532. It can be observed from the images that when the target is near the edges of the image, the reconstruction performance of the rosette sampling technique deteriorates; however, there is still significant contrast between the reconstructed target image and the background for detection of the target to be possible. The case where the target is near the outer limits of the image is rare in a typical scenario because once a target has been acquired, the tracking logic continually tries to keep the target near the center of the FOV. As the target moves to the center, the reconstruction performance improves and the level-of-detail of the target significantly increases. The performance of the proposed technique compared to the baseline techniques is discussed in the next section.

4.2 *Performance Comparison with Baseline Techniques*

The reconstructed images obtained using the rosette scanning pattern, the random Bernoulli, and the random Gaussian sampling technique are shown in Fig. 8 for different numbers of samples taken from the test image. The test image used in the reconstruction is given in Fig. 5(a). By visual inspection it can be observed that the rosette sampling technique provides a better reconstruction performance, especially with a lower number of samples. The targets are clearly distinguishable in the reconstructed images with the rosette sampling technique even with a small number of samples.

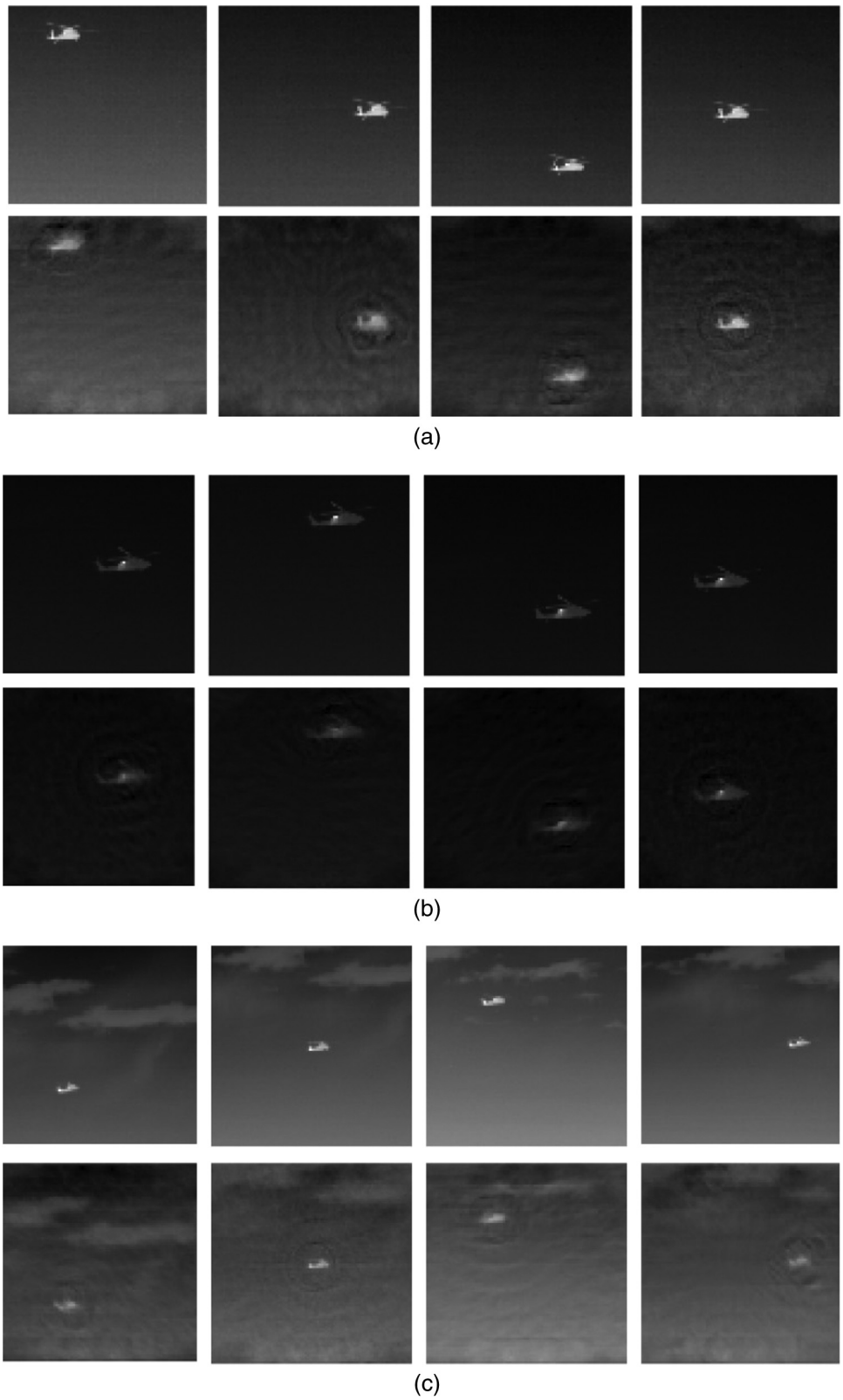

Fig. 7 The test images (top rows) and images reconstructed with the rosette scanning pattern (bottom rows), for (a) a high contrast scenario, (b) a low contrast scenario, and (c) a scenario with background clutter; for different target sizes and target locations within the FOV in each scenario.

In Fig. 9, some test images captured with an IR camera and the reconstructed images are presented for the case when 2532 samples are taken from the image. In Fig. 9, the top image is the original test image to be reconstructed, and the images reconstructed with the rosette, random Bernoulli, and random Gaussian sampling measurement matrices are given from the second row to the bottom, respectively. These test images have different characteristics

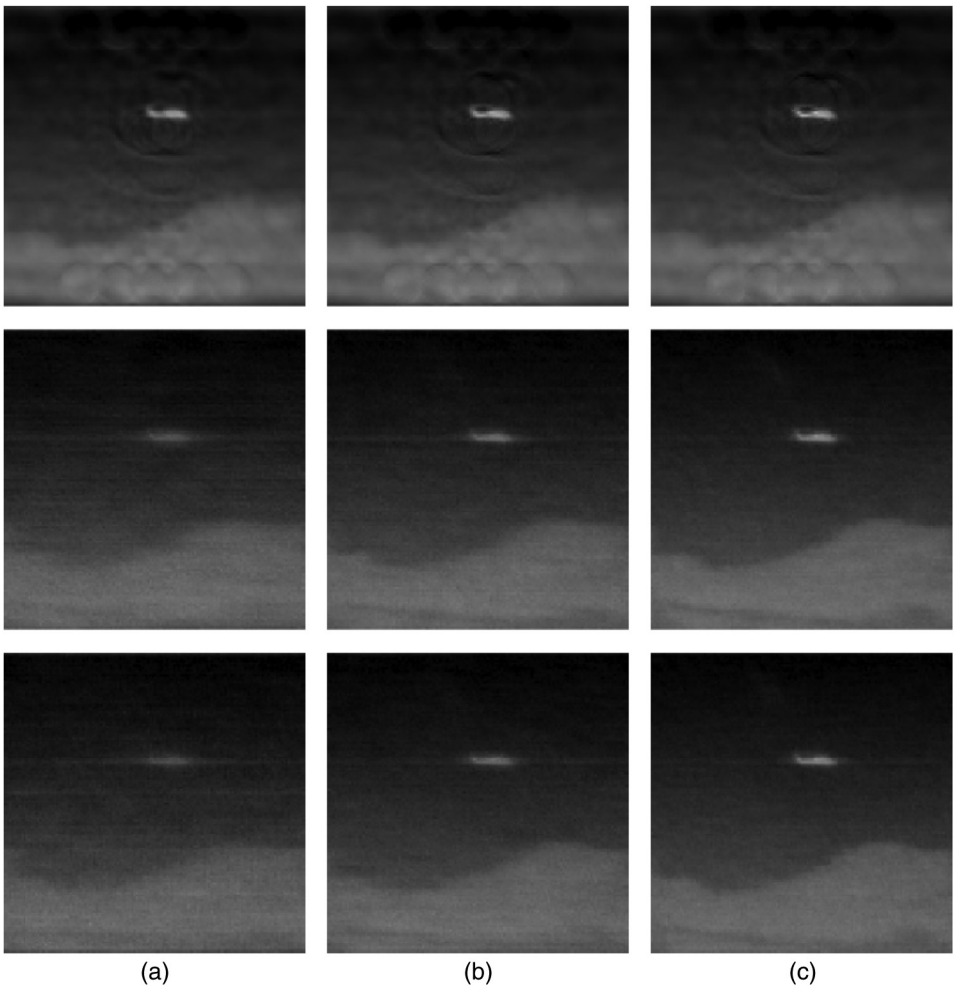

Fig. 8 The reconstructed images for the rosette scanning pattern, random Bernoulli, and random Gaussian measurement matrices, from top to bottom, respectively, for (a) 1588 samples, (b) 2532 samples, and (c) 4082 samples.

such that target location, target orientation, and the background differ significantly. In Fig. 10, we repeat the previous experiment shown in Fig. 9 with synthetic IR images of a helicopter which also contain flares in certain instances.

It can be observed from the figures that when the target is near the center, the reconstruction performance of the rosette measurement matrix is better than that of the random Bernoulli or random Gaussian sampling strategies. This is also the case when there is a flare present in the scene. Up to this point, the assessment of performance has been conducted visually, based on target/background separability and the level of target detail present in the reconstructed image.

The recovered images using different sampling strategies can also be compared in terms of "quality." The term quality is a perceptual phenomenon and in order to quantify this subjective quality term, objective image quality measures are used. Therefore, for the comparison of the quality of the reconstruction performance of the sampling techniques, average peak signal-to-noise ratio (PSNR) and "universal image quality index" (UIQI)[30] measures are used. PSNR measure is the natural extension of the mean squared error (MSE). The MSE and PSNR measures are defined in Eq. (6), where x denotes the original test image which has been vectorized and x_{recons} denotes the reconstructed signal, both of size $N \times 1$. Since the IR images used have been normalized to the [0,1] interval, $\max(x)$ is equal to one.

$$\text{MSE} = \frac{1}{N}\sum_{i=1}^{N} |x(i) - x_{\text{recons}}|^2,$$

$$\text{PSNR} = 10\log_{10}\left(\frac{\max(x)^2}{\text{MSE}}\right) = 10\log_{10}\left(\frac{1}{\text{MSE}}\right). \tag{6}$$

The other performance measure used in the experiments is the UIQI, which is computed as

$$Q = \left(\frac{\sigma_{XX_{\text{recons}}}}{\sigma_X \sigma_{X_{\text{recons}}}}\right)\left(\frac{2\bar{X}\bar{X}_{\text{recons}}}{\bar{X}^2 + (\bar{X}_{\text{recons}})^2}\right)\left(\frac{2\sigma_X \sigma_{X_{\text{recons}}}}{\sigma_X^2 + \sigma_{X_{\text{recons}}}^2}\right). \tag{7}$$

Here, $\sigma_{XX_{\text{recons}}}$ denotes the cross-correlation between the original image (X) and the reconstructed image X_{recons}, and σ_X and $\sigma_{X_{\text{recons}}}$ are the standard deviations of the original and the reconstructed images, respectively. The mean values of the original and the reconstructed images are denoted by $\bar{X}$ and $\bar{X}_{\text{recons}}$. The quality of the reconstructed image is incorporated into the quality index measure by the evaluation of "loss of correlation," "luminance distortion," and "contrast

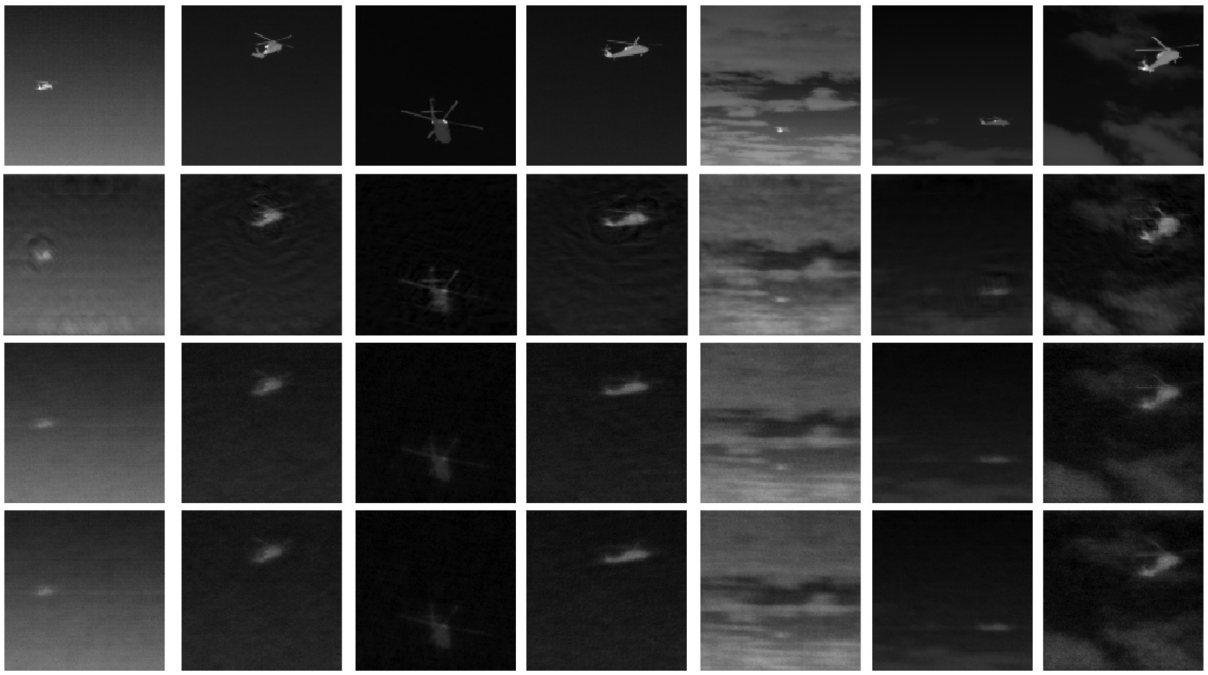

Fig. 9 The nonsynthetic test images (top row) and reconstructed images for the rosette scanning pattern, random Bernoulli, and random Gaussian measurement matrices, from top to bottom, respectively.

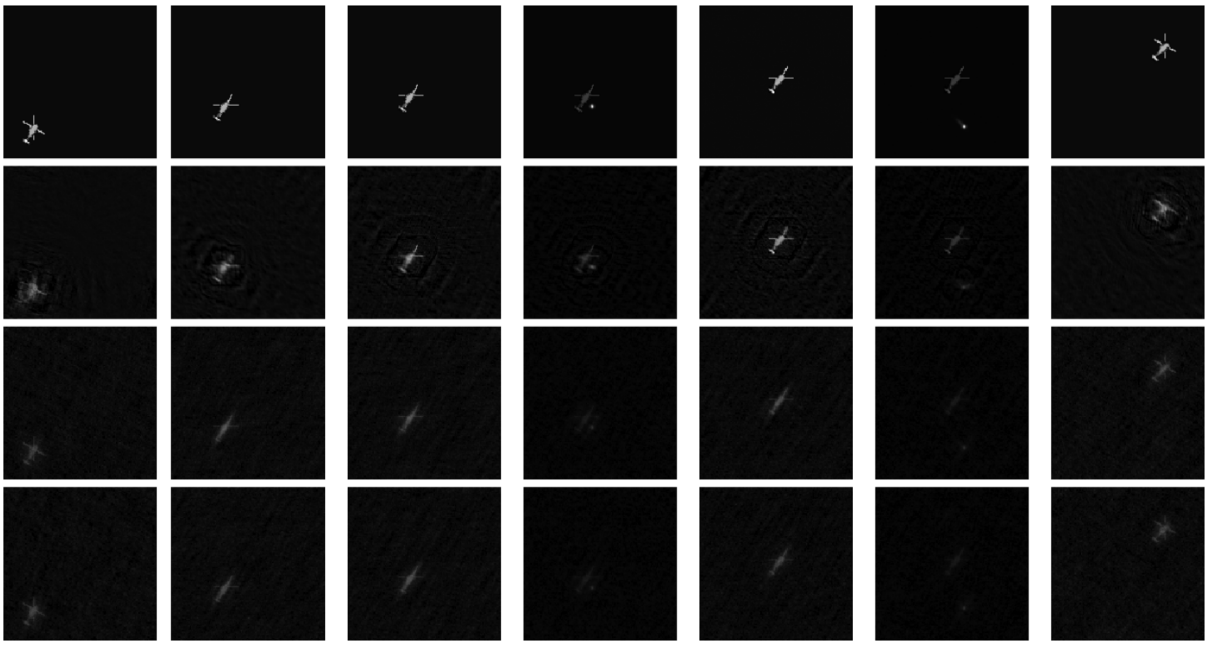

Fig. 10 The synthetic test images (top row) and reconstructed images for the rosette scanning pattern, random Bernoulli, and random Gaussian measurement matrices, from top to bottom respectively, with and without flares.

distortion" terms,[30] which are multiplicatively combined in Eq. (7). The UIQI measure takes values between the $[-1,1]$ interval such that the quality index becomes one if the input image and reconstructed image are identical. Therefore, a higher value of quality index is a simple indicator of better sparse image recovery. To use this measure in the experiments, the reconstructed signal is reshaped as a matrix to form the reconstructed image X_{recons}, which is of size 128×128 pixels.

Average PSNR and UIQI values for the sampling strategies considered are shown in Tables 1 and 2 for the different datasets and for different numbers of samples.

By looking at the results presented in Table 1, it can be observed that the proposed scheme achieves comparable results with the baseline sampling strategies in nonsynthetic images. Although the baseline sampling techniques provide higher quality measures, the proposed scheme preserves the object details and enhances the target/background

Table 1 The average PSNR and UIQI values for each sampling pattern for different numbers of samples for the image dataset captured with an IR camera.

	Average PSNR (dB)			UIQI		
Sampling method	1588 samples	2532 samples	4082 samples	1588 samples	2532 samples	4082 samples
Rosette	30.483	31.186	32.303	0.918	0.926	0.939
Random Bernoulli	31.562	33.212	35.211	0.912	0.942	0.965
Random Gaussian	31.442	33.190	35.181	0.911	0.942	0.964

Table 2 The average PSNR and UIQI values for each sampling pattern for different numbers of samples for the synthetic image dataset.

	Average PSNR (dB)			UIQI		
Sampling method	1588 samples	2532 samples	4082 samples	1588 samples	2532 samples	4082 samples
Rosette	30.475	30.700	31.228	0.596	0.625	0.673
Random Bernoulli	29.131	29.917	31.086	0.319	0.470	0.626
Random Gaussian	29.073	29.898	31.119	0.312	0.468	0.630

separability better than the baseline techniques as shown in Fig. 9 for nonsynthetic images and also in Fig. 10 for synthetic images. The quality measures try to evaluate the image quality in a comprehensive manner by defining the perceived quality on both background and foreground regions. Since the proposed sampling scheme filters the background within its IFOV as a natural outcome of its sampling behavior, the background details are lost to some extent in the reconstructed images, especially in the presence of a complex background. Therefore, the rosette sampling method does not provide higher results on the image quality metrics. In the performance tests carried out for synthetic imagery which contain low levels of background detail, the proposed scheme outperforms the baseline sampling regimes as

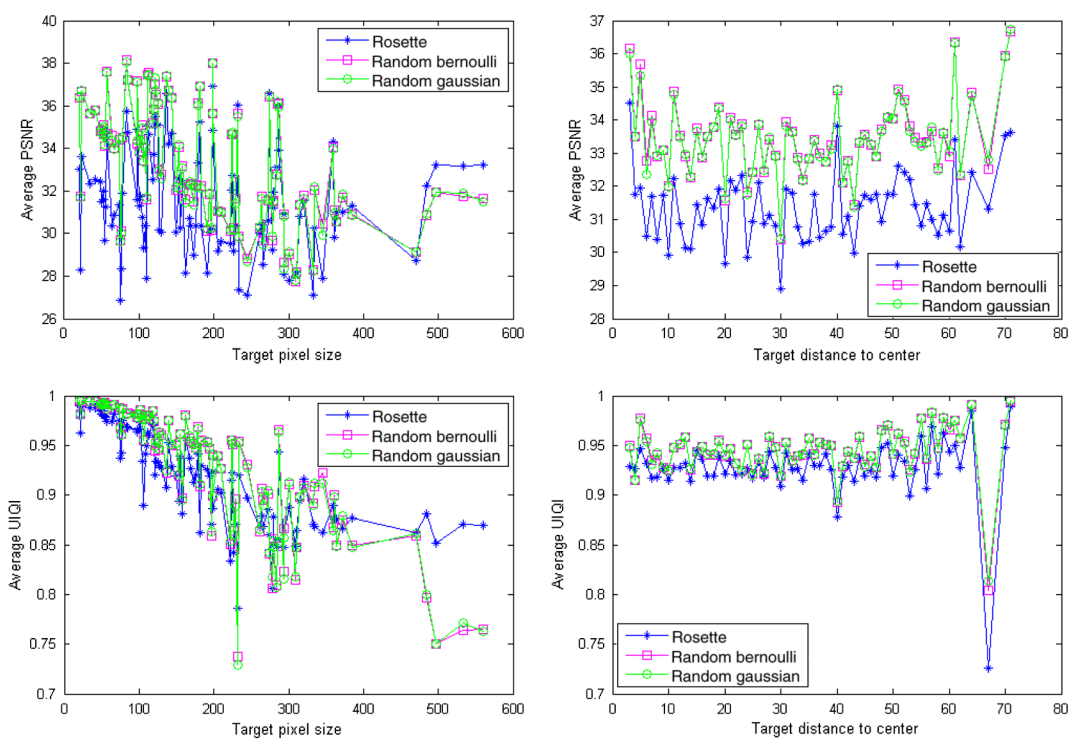

Fig. 11 Reconstruction performance with respect to target's size and target's distance for the dataset captured with an IR camera.

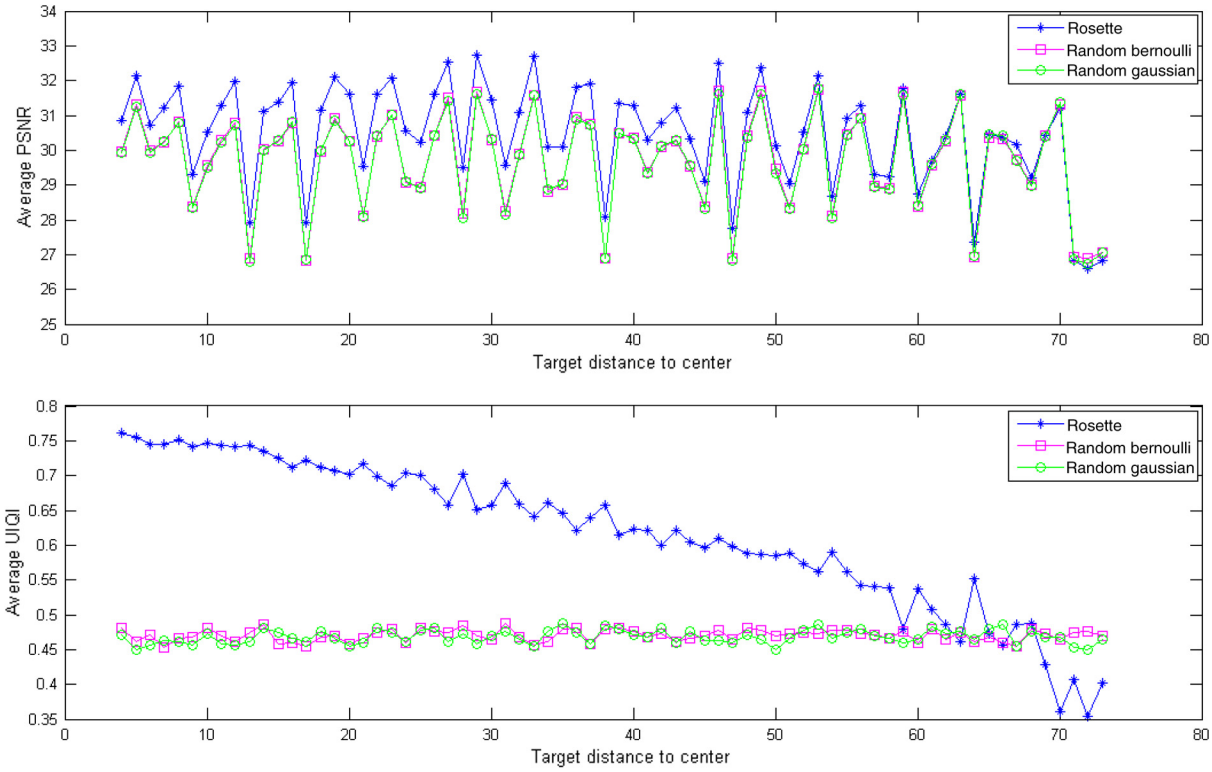

Fig. 12 Reconstruction performance with respect to target's size and target's distance for the synthetic IR image dataset.

presented in Table 2. The method achieves a better target representation by obtaining a higher level of target detail and contrast.

In the test image datasets, the location and the size of the target in the images vary within the FOV. Therefore, it is meaningful to provide performance comparison with respect to the target's size in pixels and its distance from the image center. For this purpose, we provide the PSNR and UIQI performance comparisons of each method with respect to the target's size and target distance when 2532 samples are taken from the image as shown in Fig. 11. We also provide the PSNR and UIQI performance comparisons in Fig. 12 for each method with respect to target distance for the synthetic image dataset because the target size does not vary very much within this dataset.

It can be observed from Figs. 11 and 12 that the rosette sampling strategy behaves in a similar fashion compared to the baseline techniques. In terms of PSNR and UIQI, there does not seem to be a strong dependence on target size and location in Fig. 11, although this is not strictly consistent with the visual observations. In Fig. 12, there does not seem to be a dependency on target location in the PSNR and UIQI metrics for the random Gaussian and random Bernoulli sampling methods. For the rosette sampling method, the dependency is present in the UIQI metric, but not in the PSNR metric. If we consider the coverage provided by the IFOV regions, it can be seen that when the target is close to the center, the IFOV regions will sample the target at multiple locations. This is true regardless of target size because even if the target is larger than the IFOV, it will be sampled by the IFOV numerous times.

The aim of this section was to demonstrate that a comparable performance may be achieved with the rosette scanning pattern for the reconstruction of images. The images reconstructed with samples taken with the rosette scanning pattern provide sufficient contrast for target detection/tracking applications regardless of target size/location and the fact that the loss of performance in terms of objective quality measures (PSNR and UIQI) is not very critical for these applications. Furthermore, it may be observed from the reconstructed images that the proposed scheme preserves object details in the scene and target/background contrast, but due to its scanning characteristics, it loses some information especially in the image regions that have complex background. The quality scores are directly affected by these information loses, but the reconstructed images using the rosette pattern provide better contrast and target representation that are more crucial in target detection and tracking applications.

The reconstruction problem solved using the SPGL1 library is run on a personal computer which has an Intel®i7 3.4 GHz processor and 8 GB RAM. The algorithms are implemented in MATLAB® and have not been optimized for computational efficiency. The average reconstruction time of an image using the rosette sampling technique is ~90, 120, and 180 s for 1588, 2532, and 4082 samples, respectively.

5 Conclusions and Future Work

In this paper, a framework for transforming the samples taken by the rosette scanning seeker into images via CS is proposed. Rosette scanning seekers take samples from the scene through their scanning pattern, but rather than forming

an image with these samples, they employ various signal processing methods to estimate the target location. For these scanning systems, CS offers a way to perform target detection and tracking similar to an imaging system. The reconstructed images from samples obtained via the rosette scanning pattern using the CS framework are of sufficient quality in terms of PSNR and UIQI. Thus, the rosette scanning architecture used with the CS framework shows promise in the realization of an imaging system using an old generation scanning system. As future work, the effects of target and missile movement will be added to the simulations so that the closed-loop missile simulation performance can be analyzed.

References

1. D. L. Donoho, "Compressed sensing," *IEEE Trans. Inf. Theory* **52**, 1289–1306 (2006).
2. E. Candes, J. Romberg, and T. Tao, "Robust uncertainty principles: exact signal reconstruction from highly incomplete frequency information," *IEEE Trans. Inf. Theory* **52**, 489–509 (2006).
3. C. G. Graff and E. Y. Sidky, "Compressive sensing in medical imaging," *Appl. Opt.* **54**, C23–C44 (2015).
4. M. Lustig et al., "Compressed sensing MRI," *IEEE Signal Process Mag.* **25**(2), 72–82 (2008).
5. R. Baraniuk and P. Steeghs, "Compressive radar imaging," in *2007 IEEE Radar Conf.*, pp. 128–133 (2007).
6. R. L. Moses, L. C. Potter, and M. Cetin, "Wide-Angle SAR Imaging," *Proc. SPIE* **5427**, 164–175 (2004).
7. N. A. Goodman and L. C. Potter, "Pitfalls and possibilities of radar compressive sensing," *Appl. Opt.* **54**, C1–C13 (2015).
8. Y. Kashter, O. Levi, and A. Stern, "Optical compressive change and motion detection," *Appl. Opt.* **51**, 2491–2496 (2012).
9. X. Song, H. Yin, and Y. Yan, "Imaging method with low data rate for autonomous star trackers based on compressive sensing," *J. Electron. Imaging* **24**(2), 023024 (2015).
10. M. E. Gehm and D. J. Brady, "Compressive sensing in the EO/IR," *Appl. Opt.* **54**, C14–C22 (2015).
11. F. Magalhaes et al., "High-resolution hyperspectral single-pixel imaging system based on compressive sensing," *Opt. Eng.* **51**(7), 071406 (2012).
12. H. Pan et al., "Simultaneous spatial-temporal image fusion using Kalman filtered compressed sensing," *Opt. Eng.* **51**(5), 057005 (2012).
13. Z. Wang et al., "Superresolution imaging by dynamic single-pixel compressive sensing system," *Opt. Eng.* **52**(6), 063201 (2013).
14. S. Cakir, H. Uzeler, and T. Aytaç, "Sampling strategy for the sparse recovery of infrared images," *Appl. Opt.* **52**, 6858–6867 (2013).
15. S. Qaisar et al., "Compressive sensing: from theory to applications, a survey," *J. Commun. Networks* **15**, 443–456 (2013).
16. M. Wakin et al., "An architecture for compressive imaging," in *2006 IEEE Int. Conf. on Image Processing*, pp. 1273–1276 (2006).
17. A. Mahalanobis et al., "Recent results of medium wave infrared compressive sensing," *Appl. Opt.* **53**, 8060–8070 (2014).
18. H. K. Hong et al., "Reticles-rotating systems," Chapter in *Encyclopedia of Optical Engineering*, Vol. 3, pp. 2431–2444, Marcel Dekker, Inc., New York (2003).
19. G. Gerson and A. K. Rue, Chapter 22, *The Infrared Handbook*, pp. 51–56, Environmental Research Institute of Michigan, Washington, DC (1993).
20. H. Uzeler, S. Cakir, and T. Aytaç, "Image generation for single detector infrared seekers via compressive sensing," *Proc. SPIE* **8896**, 88960T (2013).
21. H. Uzeler, S. Cakir, and T. Aytaç, "Compressive sensing applications for single detector rosette scanning infrared seekers," *Proc. SPIE* **9648**, 964809 (2015).
22. R. Baraniuk, "Compressive sensing [lecture notes]," *IEEE Signal Process Mag.* **24**(4), 118–121 (2007).
23. E. Candes and J. Romberg, "Sparsity and incoherence in compressive sampling," *Inverse Prob.* **23**(3), 969 (2007).
24. S. G. Jahng et al., "Dynamic simulation of the rosette scanning infrared seeker and an infrared counter-countermeasure using the moment technique," *Opt. Eng.* **38**(5), 921–928 (1999).
25. S.-G. Jahng et al., "New infrared counter-countermeasure technique using an iterative self-organizing data analysis algorithm for the rosette scanning infrared seeker," *Opt. Eng.* **39**(9), 2397–2404 (2000).
26. E. Candes and J. Romberg, "L1-Magic," http://users.ece.gatech.edu/justin/l1magic/ (2005).
27. D. Donoho et al., "Sparselab" (2007), Stanford University, http://sparselab.stanford.edu.
28. E. van den Berg and M. P. Friedlander, "SPGL1: a solver for large-scale sparse reconstruction," (2007), http://www.cs.ubc.ca/labs/scl/spgl1.
29. E. van den Berg and M. Friedlander, "Probing the pareto frontier for basis pursuit solutions," *SIAM J. Sci. Comput.* **31**(2), 890–912 (2009).
30. Z. Wang and A. Bovik, "A universal image quality index," *IEEE Signal Process Lett.* **9**, 81–84 (2002).

Hande Uzeler received her BS and MS degrees in electrical and electronics engineering from Bilkent University in Ankara, Turkey, in 2007 and 2010, respectively. In 2010, she joined TÜBİTAK BİLGEM İLTAREN, where she is currently a senior research scientist working in the IR/EO technologies department. Her current research interests are infrared sensing, imaging infrared systems, and signal processing.

Serdar Cakir received his BS degree in electrical and electronics engineering from Osmangazi University and his MS degree in electrical and electronics engineering from Bilkent University in Ankara, Turkey, in 2008 and 2010, respectively. In 2010, he joined TÜBİTAK BİLGEM İLTAREN, where he is a senior research scientist. He also continues his PhD studies at Bilkent University, Department of Electrical Engineering. His main research interests are image/video processing, computer vision, pattern recognition, and infrared imagery.

Tayfun Aytaç received his BS degree in electrical and electronics engineering from Gazi University, Ankara, in 2000 and his MS and PhD degrees in electrical and electronics engineering from Bilkent University, Ankara, in 2002 and 2006, respectively. He joined TÜBİTAK BİLGEM İLTAREN in 2006, where he is currently a chief research scientist. His research interests include infrared and optical sensing, electronic warfare in infrared band, simulation and modeling of IR/EO systems, and HWIL systems.